Effects of Nonequilibrium Ablation Chemistry on Viking Radio Blackout

JOHN S. EVANS,* CHARLES J. SCHEXNAYDER JR.,* AND WILLIAM L. GROSE†
NASA Langley Research Center, Hampton, Va.

The length of the entry blackout period during descent of the Viking Lander into the Mars atmosphere is predicted from calculated profiles of electron density in the shock layer over the aeroshell. Nonequilibrium chemistry plays a key role in the calculation, both in the inviscid flow and in the boundary layer. This is especially true in the boundary layer contaminated with ablation material, for which nonequilibrium chemistry predicts electron densities two decades lower than the same case calculated with equilibrium chemistry.

Nomenclature

f = transmitter frequency, Hz
N_e = electron concentration, cm^{-3}
$(N_e)_{cr}$ = critical value of N_e, 1.24×10^{10} cm^{-3}
R_b = base radius, cm
R_n = nose radius, cm
r = perpendicular distance from symmetry axis, cm
s = distance along streamline from shock, cm
T = temperature, °K
x = distance along shock, cm
y = perpendicular distance from body surface, cm
z = distance along symmetry axis, cm
Δ = thickness of shock layer, cm

Subscript
s = value on shock

Introduction

NONEQUILIBRIUM chemistry has long been recognized as an important factor in predicting radio blackout during planetary entry.[1] More recently, it has been observed that alkali metals present in ablation products also frequently contribute heavily to production of the free electrons responsible for radio blackout. However, this conclusion was based on comparisons between observed flight experiments and calculations in which the inviscid portion of the shock layer included nonequilibrium chemistry but in which equilibrium chemistry was used for the boundary layer.[2] In this paper, nonequilibrium chemistry is used throughout the shock layer—including the boundary layer, where finite-rate ionization of the alkali metals occurs.

Mission Description

After the Viking spacecraft[3,4] is established in orbit about Mars, the lander (protected by an aeroshell) separates from the spacecraft and enters the atmosphere as it proceeds toward its landing spot on the surface. The main sequence of events is depicted in Fig. 1. Only the entry portion of the sequence is of interest here, for the friction that produces rapid deceleration also heats the gas flow over the entering vehicle and, thus, is responsible for creation of the free electrons which interfere with radio transmission. A sketch of the aeroshell and its speed and altitude as a function of time for a typical trajectory are shown in Fig. 2. The atmosphere for this trajectory is designated Max $H_{\rho,s}$ (Mars Engineering Model) and is the only one for which results are shown in this paper. Calculations were made at altitudes 57.0, 62.8, 76.5, and 82.3 km. For other trajectories considered‡ only enough calculations were made to insure

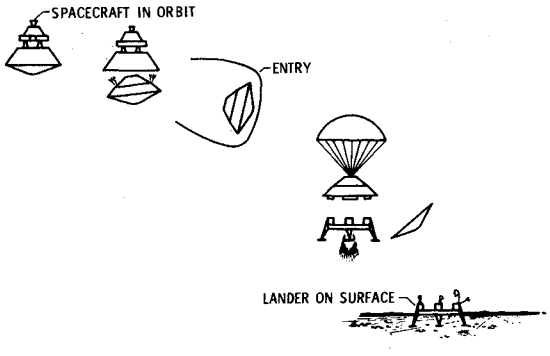

Fig. 1 Sequence of events for Viking landing.

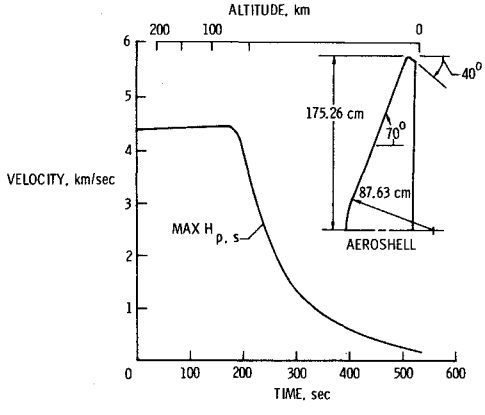

Fig. 2 Entry trajectory and aeroshell configuration; atmosphere Max $H_{\rho,s}$; entry angle = 15°; $L/D = 0.18$.

Presented as Paper 73-260 at the AIAA 11th Aerospace Sciences Meeting, Washington, D.C., January 10–12, 1973; submitted January 22, 1973; revision received September 17, 1973.

Index categories: Reactive Flows; Thermochemistry, and Chemical Kinetics.

* Aerospace Technologist, Hypersonic Vehicles Division.
† Aerospace Technologist, Space Systems Division.

‡ Since the composition of Mars' atmosphere is not known, the amounts of N_2 and Ar mixed with the main constituent, CO_2, were among the parameters used to define the trajectories.

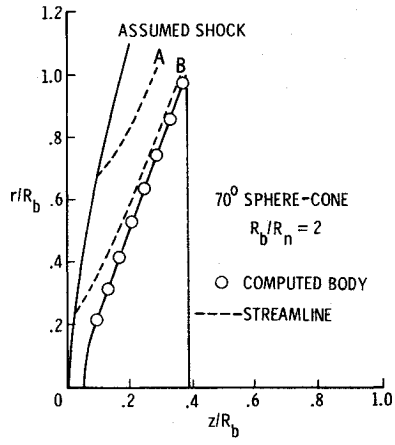

Fig. 3 Streamlines and computed body shape from inviscid flowfield calculations; alt = 62.8 km.

that the longest blackout time for the radar altimeter ($f = 1$ GHz) would occur for the one shown in Fig. 2.

Inviscid Flowfield Calculations

Inviscid flow in the shock layer was calculated by an inverse method[5] which used a finite-rate chemistry system consisting of 13 species (CO_2, CO, NO, O_2, N_2, O, N, C, Ar, NO^+, CO^+, O_2^+, e^-) and the first 19 reactions given in Table 1. For all of the calculations presented, the assumed shock shapes are described by

$$z_s = r_s^2/\alpha + \beta r_s$$

The parameter α controls the bluntness of the shock, and the parameter β is the slope of the asymptote of the shock for large values of r_s.

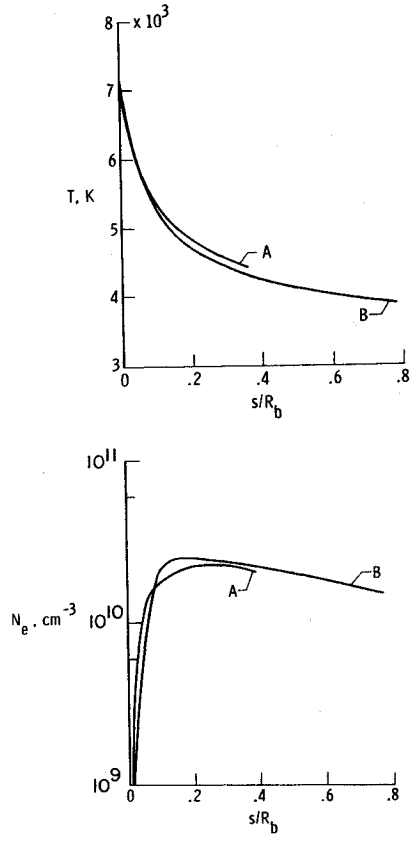

Fig. 4 Variation of T and N_e along streamlines; alt = 62.8 km.

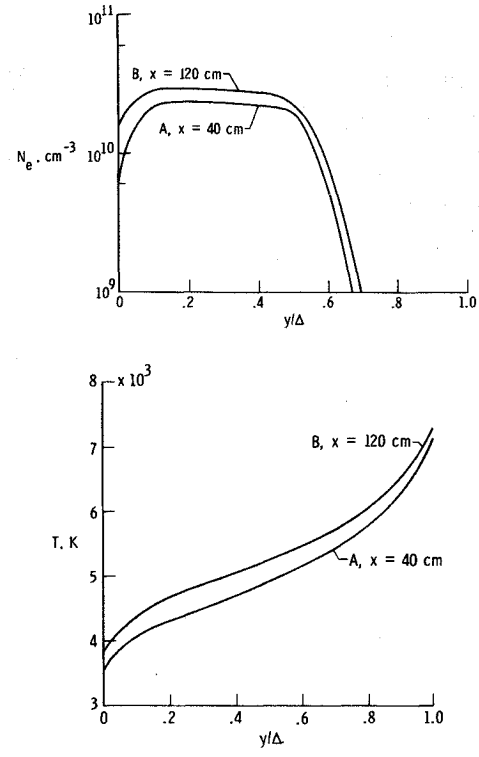

Fig. 5 Profiles T and N_e; alt = 62.8 km.

The assumed shock and the computed body for altitude = 62.8 km are shown in Fig. 3.§ The computed body adequately approximates a 70° half-angle sphere cone ($R_b/R_n = 2$), which is the shape of the aeroshell. Also shown in the figure are two typical streamlines denoted as A and B. Distributions of T and N_e along these streamlines are shown in Fig. 4. N_e increases rapidly with distance from the shock and then decreases as the flow expands and cools. Figure 5 shows profiles of T and N_e across the shock layer. Profile A originates at the shock at $x = 40$ cm; profile B originates at the shock at $x = 120$ cm. It should be noted in these figures that $y = 0$ corresponds to the inviscid body streamline. This is not the usual practice for an inverse method. However, the results are presented in this fashion in order to be consistent with subsequent boundary-layer calculations which used a body oriented coordinate system.

Boundary Layer

The same chemistry (except for the addition of the species Na and Na^+ and the reactions 20–22 in Table 1) was used to calculate the boundary layer using a laminar, finite-difference, nonequilibrium, multicomponent diffusion, boundary-layer program[6] which accounts for material added to the boundary layer by ablation of the heat shield. Changes made to adapt the program to our use were 1) reduction of storage requirement, 2) introduction of variable step size keyed to the magnitude of changes in chemical composition, 3) replacement of thermodynamic data and the reaction system, 4) replacement of the means for achieving conservation of elements, 5) introduction of the species Na and Na^+, and 6) updating the chemical reaction rates.

The reaction rates given in Table 1 are from a file of reaction rates created by the authors about a decade ago. The values in it are drawn from the literature and are continuously updated. It

§ Body shape was maintained with changing altitude by varying α and β.

Table 1 Reactions and rates used for flowfield calculations

i	Reaction	Forward rate constant[a] A	B	C	Reverse rate constant[a] A	B	C
1	$CO+m \leftrightharpoons C+O+m$	4.48×10^{19}	−1.0	128,900	1.0×10^{18}	−1.0	0
2	$N_2+m \leftrightharpoons N+N+m$	2.46×10^{19}	−1.0	113,200	1.5×10^{18}	−1.0	0
3	$NO+m \leftrightharpoons N+O+m$	4.09×10^{18}	−1.0	75,330	3.5×10^{18}	−1.0	0
4	$CO_2+m \leftrightharpoons CO+O+m$	1.20×10^{11}	0.5	34,340	2.0×10^{6}	1.25	−28,400
5	$O_2+m \leftrightharpoons O+O+m$	9.05×10^{18}	−1.0	59,370	9.0×10^{15}	−0.5	0
6	$CO+N \leftrightharpoons NO+C$	2.86×10^{11}	0.5	53,630	2.6×10^{10}	0.5	0
7	$CO+CO \leftrightharpoons CO_2+C$	2.33×10^{9}	0.5	65,710	4.6×10^{12}	−0.25	0
8	$CO+O \leftrightharpoons O_2+C$	2.73×10^{12}	0.5	69,540	9.4×10^{12}	0.25	0
9	$N_2+O \leftrightharpoons NO+N$	7.35×10^{11}	0.5	37,940	1.6×10^{11}	0.5	0
10	$NO+CO \leftrightharpoons CO_2+N$	4.59×10^{8}	0.5	12,070	9.9×10^{12}	−0.25	0
11	$NO+O \leftrightharpoons O_2+N$	2.98×10^{11}	0.5	19,460	9.5×10^{9}	1.0	0
12	$CO_2+O \leftrightharpoons O_2+CO$	2.54×10^{11}	0.5	27,690	5.0×10^{8}	1.0	23,900
13	$O+O \leftrightharpoons O_2^+ + e^-$	5.42×10^{10}	0.5	80,560	7.2×10^{20}	−1.2	0
14	$C+O \leftrightharpoons CO^+ + e^-$	7.55×10^{10}	0.5	33,660	1.08×10^{21}	−1.2	0
15	$N+O \leftrightharpoons NO^+ + e^-$	2.43×10^{10}	0.5	32,150	4.0×10^{20}	−1.2	0
16	$CO+NO^+ \leftrightharpoons CO^+ + NO$	2.30×10^{12}	0.5	55,190	1.5×10^{13}	0	0
17	$O_2+NO^+ \leftrightharpoons O_2^+ + NO$	2.20×10^{12}	0.5	32,840	4.0×10^{11}	0.5	0
18	$CO+O_2^+ \leftrightharpoons CO^+ + O_2$	2.20×10^{12}	0.5	22,400	7.0×10^{13}	0	0
19	$O+NO^+ \leftrightharpoons O_2^+ + N$	2.70×10^{12}	0.5	48,730	2.0×10^{12}	0.5	0
20	$Na+m \leftrightharpoons Na^+ + e^- + m$	2.46×10^{11}	0.5	59,670	6.0×10^{19}	−1.0	0
21	$Na^+ + NO \leftrightharpoons NO^+ + Na$	4.85×10^{10}	0.5	47,710	1.0×10^{13}	0	0
22	$Na^+ + O_2 \leftrightharpoons O_2^+ + Na$	4.80×10^{10}	0.5	79,410	1.0×10^{13}	0	0

[a] Form of rate constant is $k = AT^B \exp(-C/T)$ with k in cm^3-$mole^{-1}$-sec^{-1} or cm^6-$mole^{-2}$-sec^{-1}

would be both impractical and inaccurate to attempt to give a source for each reaction, but among the sources used were Refs. 7–23. When no literature values were found (rates 7, 10, and 20–22), the forward value of C was deduced from net change in chemical bond energy, and the remaining constants were assigned by analogy with known rates of a similar kind. The list of reaction rates is fairly long, since it was found that O_2^+ was almost as plentiful as NO^+, and that CO^+, while less important than O_2^+ and NO^+, was not always negligible. Reaction 15 was the largest source of NO^+, reaction 13 of O_2^+, and reaction 14 of CO^+. It should be noted that these ions are all formed by associative ionization of atoms, and therefore require that the reaction system be able to supply atoms at adequately high rates at the relatively low temperatures of the Viking entry to Mars. The shuffle reactions (6–11) are better atom sources than the dissociation reactions (1–5).

Information about the injection rate of ablation material into the boundary layer and about its alkali metal content were obtained from Martin Marietta Corp. through the Viking Project Office at Langley Research Center. For given altitude, a constant injection rate was used throughout the boundary layer, that is, (57.0, 0.537), (62.8, 0.493), (76.5, 0.49), (82.3, 0.298), where the first number is altitude in km and the second is mass injection rate in kg sec^{-1} m^{-2}. For all altitudes, 1000 parts per million by weight of the injected material were taken to be Na, and the remainder were treated as having the composition of the Mars ambient atmosphere. The composition of the Mars ambient atmosphere in the Max $H_{\rho,s}$ model is (CO_2, 0.815), (N_2, 0.01), (Ar, 0.175), where the numbers are mass fractions.

Edge conditions for the boundary layer were obtained from profiles of inviscid properties by reading off values at a distance from the surface equal to the boundary-layer thickness and then repeating the procedure until no significant change in boundary-layer thickness was obtained. Convergence was rapid. Displacement thickness corrections to the body shape were calculated but proved to be negligible.

Results and Discussion

The beginning point for theoretical prediction of N_e profiles is calculation of the inviscid flowfield. This is followed by calculation of the boundary layer—with and without the presence of ablation material.¶

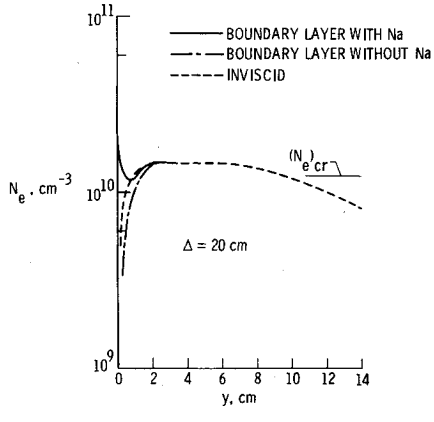

Fig. 6a N_e profiles at the radar altimeter station; $x = 91$ cm, alt = 57.0 km, velocity = 3.97 km sec^{-1}.

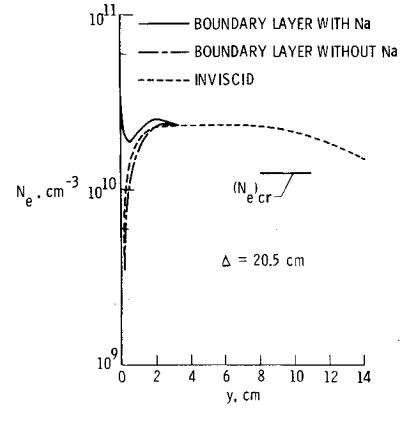

Fig. 6b N_e profiles at the radar altimeter station; $x = 91$ cm, alt = 62.8 km, velocity = 4.18 km sec^{-1}.

¶ Comparison of the calculations made with and without ablation material permits one to see the effect of contamination.

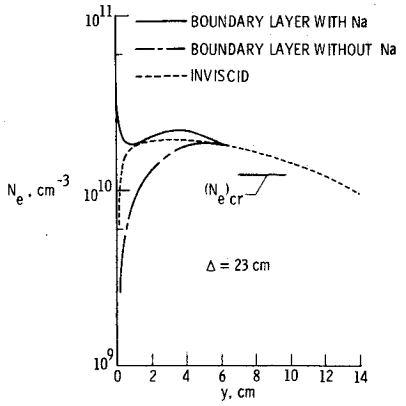

Fig. 6c N_e profiles at the radar altimeter station; $x = 91$ cm, alt = 76.5 km, velocity = 4.38 km sec^{-1}.

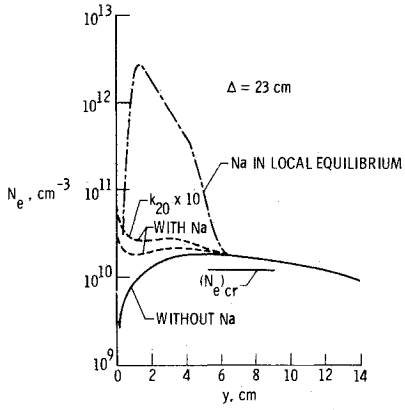

Fig. 7 Comparison of equilibrium and nonequilibrium N_e profiles; alt = 76.5 km, velocity = 4.38 km sec^{-1}.

Figure 6 shows calculated N_e profiles at four altitudes for the radar altimeter station. Note that the largest boundary-layer corrections to the inviscid profiles are at the highest altitudes. This is to be expected, since boundary-layer thickness grows with altitude. Next, note that without the presence of contamination, the boundary-layer calculations yield small values of N_e near the wall and that the extent of this wall effect grows larger with increase in altitude. When ablation products are included the situation reverses; N_e is largest near the wall where the concentration of ablated material is highest.

An interesting and practical point is brought out in Fig. 7, where three calculated versions of a contaminated boundary-layer profile are shown—two for nonequilibrium chemistry and the other for $Na \rightarrow Na^+ + e^-$ (rate 20 in Table 1) in equilibrium at local temperature and pressure. It is seen that the older and more easily performed procedure of assuming local equilibrium for ionization of the sodium yields a much higher concentration of electrons than the nonequilibrium calculations. The large difference between the values of peak N_e calculated by the two methods can also be seen in Fig. 8, where peak N_e from profiles like those in Fig. 7 are plotted against time.

For those who plan planetary entry missions, the important question which must be answered is, "What is the period of time during entry that the radio transmission will be blacked out?" Figure 9 attempts to answer this question for the Viking radar altimeter beam as directly as possible. The radar altimeter will black out for approximately 40 sec beginning about 160 sec after entering the Martian atmosphere, provided that the entry speed is 4.63 km sec^{-1}, the entry angle is $-15°$, and the Martian atmosphere is accurately described by the Max $H_{\rho,s}$ model. Other answers can be given for different input numbers, but if the input is limited to the 11 cases listed in the Mars Engineering Model and the rates in Table 1 are used, the results shown in Fig. 9 give the longest blackout period.

The curves of signal loss in decibels shown in Fig. 9 were calculated from profiles like those shown in Fig. 7 using the plane wave propagation theory of Swift and Evans.[24]

The middle curve shows the signal loss calculated with ablation material, the one above it shows the effect of increasing the sodium ionization rate by a factor** of 10, and the one below it shows the signal loss calculated for a clean plasma—without ablation material in the boundary layer.

When finite-rate reactions are used, the question of errors introduced by incorrect values of rates arises. The question is not easily answered, because many rates are either poorly known or have not been investigated at all. The curves in Fig. 7 can be used to illustrate this point. Two nonequilibrium curves with Na present are shown. One shows the profile as calculated with the chemistry defined in Table 1. The other shows the effect of increasing the rate for ionization of Na by a factor of 10. The profile for the faster rate lies closer to the equilibrium curve, as expected. The effect on signal loss of increasing rate 20 appears in Fig. 9, where it can be seen that there is practically no change in the emergence from blackout at around 200 sec. However, there is an earlier onset of blackout which

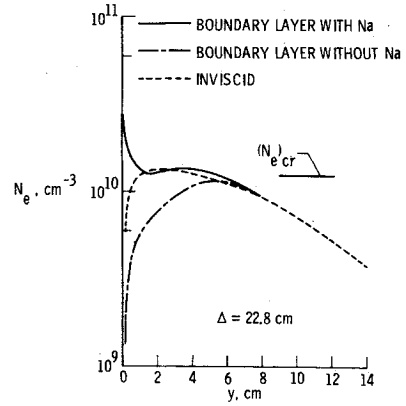

Fig. 6d N_e profiles at the radar altimeter station; $x = 91$ cm, alt = 82.3 km, velocity = 4.40 km sec^{-1}.

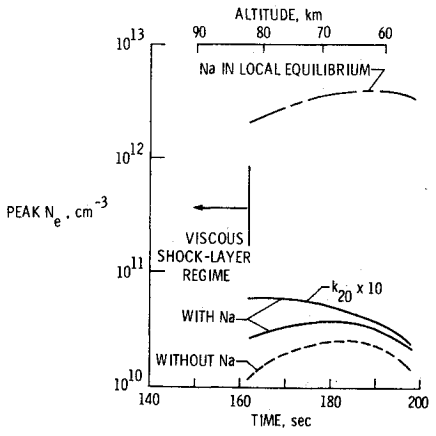

Fig. 8 Variation of peak N_e with time and altitude.

** Comparison of calculated and flight-measured values of N_e from RAM C-III data shows best agreement for the value of k_{20} used in this report, but a value of k_{20} up to 10 times faster would agree reasonably well, also.

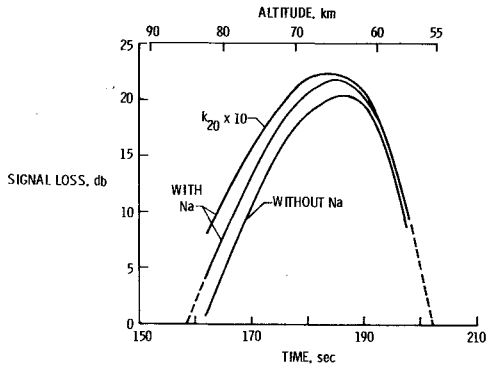

Fig. 9 Signal loss variation with time and altitude.

has not been calculated because the boundary layer fills the shock layer at altitudes above about 82 km, as is indicated in Fig. 8.

Conclusions

Blackout time for the Viking radar altimeter is calculated to be around 40 sec, beginning about 160 sec after entry into the Mars atmosphere. With the given set of reaction rates, this 40-sec interval is the longest blackout time anticipated. However, should the ionization rate for sodium, $Na \rightarrow Na^+ + e^-$, be faster by a factor of 10 than the rate used, then the onset of blackout would occur earlier without any appreciable change in the time when blackout is over. The increased length of the blackout period for this circumstance was not determined, since the boundary-layer analysis used becomes invalid at the highest altitudes for which calculations are needed.

Of course, it should be remembered that there may be no blackout of the radar altimeter. The composition of Mars' atmosphere is still uncertain, and there is a range of possible entry trajectories. The objective of the study was to calculate the maximum blackout time which could occur, but to avoid making unrealistic assumptions which would lead to overprediction. For example, it was demonstrated that the procedure of assuming equilibrium ionization of Na leads to a large overprediction of blackout duration.

References

[1] Evans, J. S. and Huber, P. W., "Calculated Radio Attenuation Due to Plasma Sheath on Hypersonic Blunt-Nosed Cone," TN D-2043, Dec. 1963, NASA.

[2] Huber, P. W., Evans, J. S., and Schexnayder, C. J., Jr., "Comparison of Theoretical and Flight-Measured Ionization in a Blunt Body Re-Entry Flowfield," *AIAA Journal*, Vol. 9, No. 6, June 1971, pp. 1154–1162.

[3] The Viking Project Management, "1973 Viking Voyage to Mars," *Astronautics and Aeronautics*, Vol. 7, No. 11, Nov. 1969, pp. 30–59.

[4] Martin, J. S., "Mars Exploration with Viking," Tenth Space Congress, April 1973, Cocoa Beach, Florida.

[5] Grose, W. L., "A Thin-Shock-Layer Solution for Nonequilibrium, Inviscid Hypersonic Flows in Earth, Martian and Venusian Atmospheres," TN D-6529. Dec. 1971, NASA.

[6] Blottner, F. G., "Prediction of Electron Density in the Boundary Layer on Entry Vehicles With Ablation," *The Entry Plasma Sheath and its Effects on Space Vechicle Electromagnetic Systems, Vol. I*, NASA SP-252, 1971, pp. 219–240.

[7] McKenzie, R. L., "An Estimate of the Chemical Kinetics Behind Normal Shock Waves in Mixtures of Carbon Dioxide and Nitrogen for Conditions Typical of Mars Entry," TN D-3287, Feb. 1966, NASA.

[8] Dunn, M. G., "Experimental Plasma Studies," CR-1958, March 1972, NASA.

[9] Sulzmann, K. G. P., Myers, B. F., and Bartle, E. R., "CO Oxidation. Part I: Induction Period Preceding CO_2 Formation in Shock-Heated CO–O_2–Ar Mixtures," *Journal of Chemical Physics*, Vol. 42, No. 11, June 1, 1965, pp. 3969–3979.

[10] Fairbairn, A. R., "The Dissociation of CO," Research Rept. 305, Dec. 1968, Avco-Everett Research Lab., Everett, Mass.

[11] Dunn, M. G. and Lordi, J. A., "Measurement of Electron Temperature and Number Density in Shock-Tunnel Flows. Part II: $NO^+ + e^-$ Dissociative Recombination Rate in Air," *AIAA Journal*, Vol. 7, No. 11, Nov. 1969, pp. 2099–2104.

[12] Dunn, M. G., "Measurement of $C^+ + e^- + e^-$ and $CO^+ + e^-$ Recombination in Carbon Monoxide Flows," *AIAA Journal*, Vol. 9, No. 11, Nov. 1971, pp. 2184–2191.

[13] Dunn, M. G. and Lordi, J. A., "Measurement of $O_2^+ + e^-$ Dissociative Recombination in Expanding Oxygen Flows," *AIAA Journal*, Vol. 8, No. 4, April 1970, pp. 614–618.

[14] Lin, S. C. and Teare, J. D., "Rate of Ionization Behind Shock Waves in Air. II. Theoretical Interpretations," *The Physics of Fluids*, Vol. 6, No. 3, March 1963, pp. 355–375.

[15] Hansen, C. F., "Estimates for Collision-Induced Dissociation Rates," *AIAA Journal*, Vol. 3, No. 1, Jan. 1965, pp. 61–66.

[16] Byron, S., Foster, R. M., and Masson, B. S., "Flow Field Computations for Blunt Bodies in Planetary Environments," CR-106081, April 1968, NASA.

[17] Fisburne, E. S., Bilwakesh, K. R., and Edse, R., "Chemical Kinetics of Entry into the Martian Atmosphere," ARL 67-0113, May 1967, The Ohio State Univ. Aeronautical and Astronautical Research Lab., Columbus, Ohio.

[18] "Radiative Energy Transfer on Entry into Mars and Venus," NASA CR-100897, March 1969, IIT Research Institute, Chicago, Ill.

[19] Wray, K. L., "Chemical Kinetics of High Temperature Air," Research Rept. 104, June 1961, Avco-Everett Research Lab., Everett, Mass.

[20] Heicklen, J., "Gas-Phase Chemistry of Re-Entry," *AIAA Journal*, Vol. 5, No. 1, Jan. 1967, pp. 4–15.

[21] Bortner, M. H., "A Review of Rate Constants of Selected Reactions of Interest in Re-Entry Flow Fields in the Atmosphere," TN 484, May 1969, National Bureau of Standards, Washington, D.C.

[22] Dunn, M. G., "Reaction Rate Constants for Ionized Air," CAL Rept. AI-218-A-1, April 1966, Calspan Corp., Buffalo, N.Y.

[23] Appleton, J. P., Steinbery, M., and Liquornik, D. J., "Shock-Tube Study of Carbon Monoxide Dissociation Using Vacuum-Ultraviolet Absorption," *Journal of Chemical Physics*, Vol. 52, No. 5, March 1, 1970, pp. 2205–221.

[24] Swift, C. T. and Evans, J. S., "Generalized Treatment of Plane Electromagnetic Waves Passing Through an Isotropic Inhomogeneous Plasma Slab at Arbitrary Angles of Incidence," TR R-172, Dec. 1963, NASA.